

CHAPTER 2

An experimental study of the grain-scale processes of peridotite melting: implications for major and trace element distribution during equilibrium and disequilibrium melting

Mauro Lo Cascio¹

Yan Liang¹, Nobumichi Shimizu², and Paul C. Hess¹

¹Department of Geological Sciences, Brown University

Providence, Rhode Island 02912

²Geology and Geophysics, Woods Hole Oceanographic Institute,

Woods Hole, MA 02543

Published in **Contributions to Mineralogy and Petrology**, : , 2008

DOI: 10.1007/s00410-007-0275-8

Abstract

The grain-scale processes of peridotite melting were examined at 1340°C and 1.5 GPa using reaction couples formed by juxtaposing pre-synthesized clinopyroxenite against pre-synthesized orthopyroxenite or harzburgite in graphite and platinum-lined molybdenum capsules. Reaction between the clinopyroxene and orthopyroxene-rich aggregates produces a melt-enriched, orthopyroxene-free, olivine + clinopyroxene reactive boundary layer. Major and trace element abundance in clinopyroxene vary systematically across the reactive boundary layer with compositional trends similar to the published clinopyroxene core-to-rim compositional variations in the bulk lherzolite partial melting studies conducted at similar P–T conditions. The growth of the reactive boundary layer takes place at the expense of the orthopyroxenite or harzburgite and is consistent with grain-scale processes that involve dissolution, precipitation, reprecipitation, and diffusive exchange between the interstitial melt and surrounding crystals. An important consequence of dissolution–reprecipitation during crystal melt interaction is the dramatic decrease in diffusive reequilibration time between coexisting minerals and melt. This effect is especially important for high charged, slow diffusing cations during peridotite melting and melt-rock reaction. Apparent clinopyroxene–melt partition coefficients for REE, Sr, Y, Ti, and Zr, measured from reprecipitated clinopyroxene and coexisting melt in the reactive boundary layer, approach their equilibrium values reported in the literature. Disequilibrium melting models based on volume diffusion in solid limited mechanism are likely to significantly underestimate the rates at which major and trace elements in residual minerals reequilibrate with their surrounding melt.

1. Introduction

Partial melting of the Earth's mantle occurs predominantly in the spinel lherzolite stability field, where clinopyroxene (cpx) and orthopyroxene (opx) are consumed to produce olivine and basaltic melt, i.e., $\text{cpx} + \text{opx} \rightarrow \text{olivine} + \text{melt}$ (e.g., Walter, 2005 and references therein). Although the stoichiometry and melt composition of this reaction has been extensively studied, the grain-scale processes through which pyroxenes undergo partial melting have not yet been examined in detail. These processes are extremely important in controlling how major and trace elements are redistributed between the liquid product and the residual solids during partial melting, melt transport, and melt-rock reaction in the Earth's mantle. To date, most partial melting studies make two common assumptions: (1) equilibration is taken for granted when the melt composition does not change with time even though residual pyroxenes are zoned, and (2) the observed zonations in the pyroxenes are attributed to solid state diffusion. The implications of these assumptions have important consequences beyond laboratory experiments. For instance, diffusion in minerals has often been taken as the dominant rate limiting mechanism for crystal-melt chemical exchange for the trace elements during fluid or melt infiltration, melt-rock reaction, and disequilibrium melting in the upper mantle and lower crust (e.g., Navon and Stolper, 1987; Bodinier et al. 1990; Qin, 1992; Iwamori, 1993, 1994; Hauri, 1997; Korenaga and Kelemen, 1998; Van Orman et al., 2002a; Liang, 2003a). It has been shown that diffusion in solid dominated crystal-melt exchange is important for the slow diffusing trace elements only when the major element in the crystals and their coexisting melt are in chemical equilibrium (e.g., Liang, 2003b).

In a series of numerical and theoretical studies of the grain-scale kinetics of crystal dissolution in molten and partially molten systems, we have shown that dissolution, precipitation, and reprecipitation are inevitable consequences of crystal-melt interaction in

multicomponent partially molten systems (Liang, 2003b, 2005). The processes of dissolution and reprecipitation can be illustrated with the help of a simplified binary phase diagram (Fig. 1). As shown in Fig. 1, if the interstitial melt (L) is initially under-saturated with respect to the solid solution-forming crystal (S), the crystal will dissolve, but only at earlier times. Because the rate of diffusion in the melt is much faster than the rate of diffusion in the solid, the bulk melt composition quickly evolves to the liquidus of the dissolving crystal (L_e). Since only the surface of the dissolving crystal (S_e) is in chemical equilibrium with melt L_e , the interior of the crystal appears over-saturated with respect to the melt. Dissolution then reverses to precipitation that finally stops when the concentration gradients in the solid are eliminated (animations showing the processes of dissolution and reprecipitation in a crystal-melt aggregate can be found in Liang, 2003b). When the crystal-melt aggregate is open to mass transfer with their surrounding (via diffusion and advection), reprecipitation can also take place in another part of the system, away from where dissolution originated. In systems where mineral grain size is not uniform, small grains may dissolve completely before reprecipitation starts, resulting in a reduction in crystal number density. Depending on the extent of undersaturation, the reprecipitated mineral grain size may be considerably larger, as will be shown in this study. The rate of dissolution is determined by the rate of the slowest major diffusing component in the melt (usually SiO_2 , referred to as Regime I dissolution in Liang, 2003b), whereas the rate of reprecipitation is dominated by the rate of the fastest major diffusing component in the crystal. An important consequence of dissolution and reprecipitation is the acceleration of crystal-melt re-equilibration rates for both major and trace elements in partially molten silicates. This point will be further demonstrated experimentally in the present study.

In a preliminary study, we examined the major element chemistry and the kinetics of reaction between a clinopyroxenite and a harzburgite at 1340°C and 1.5 GPa using a reaction

couple method (Lo Cascio et al., 2004). The basic idea behind our reaction couple method is that if peridotite melting takes place through the reaction $\text{cpx} + \text{opx} \rightarrow \text{olivine} + \text{melt}$, the melting process then can be conveniently studied by examining the reaction between a cpx-rich aggregate and an opx-rich aggregate. Indeed, reaction between the clinopyroxenite and the harzburgite produced a reactive boundary layer (RBL) that consists of new olivine, new cpx, and melt. The formation of the RBL is consistent with a grain-scale process that involves dissolution of cpx and opx, precipitation of olivine, and reprecipitation of cpx. Major element variations of cpx across the RBL are similar to the core-to-rim compositional trends observed in cpx from bulk lherzolite partial melting studies, suggesting that the grain-scale mass transfer processes during bulk lherzolite melting in the laboratory and natural are governed by the same dissolution and reprecipitation processes documented in our reaction couple experiments. The grain size of the reprecipitated cpx (up to 50 μm long) and melt pocket (over 100 μm wide) in the RBL are sufficiently large that it would be possible to measure the REE and other incompatible trace element abundance in coexisting cpx and melt in the RBL using an ion microprobe.

In this study, we further expanded our experimental investigation of the grain-scale processes associated with peridotite melting by reacting presynthesized clinopyroxenite with presynthesized orthopyroxenite, by including spinel and small amount of basaltic melt in our reacting couple, and by analyzing both major and trace element (REE, Y, Sr, Ti, and Zr) abundance in coexisting phases in our reaction products. Since kinetic processes are path dependent and the geometry of the reaction couple in our earlier experiments (clinopyroxenite against harzburgite, Lo Cascio et al., 2004) are significantly different from that of the bulk peridotite melting studies, it is important to check if the grain scale processes summarized above and outlined in Lo Cascio et al. (2004) are sensitive to the choices of reaction couples, as well as the presence of spinel. The general conclusions of

Lo Cascio et al. (2004) may not be applicable to peridotite melting in the mantle if the grain-scale melting processes are sensitive to (or different among) the choices of reaction couples. As will be shown below this is not the case. Spinel is the main Al-bearing mineral in spinel peridotite and including spinel in our reaction couple experiments will allow us to explore the distribution of Al_2O_3 in reprecipitated cpx. Addition of small amount of basalt not only further increases the Al content of the starting material but also speed up reaction rates.

It is well known that partition coefficients of REE and high field strength elements (HFSE) between cpx and coexisting basaltic liquid depend strongly on the Al_2O_3 abundance in cpx (e.g. Lundstrom et al., 1994; Gaetani and Grove, 1995; Hill et al., 2000). Measuring REE and selected incompatible trace element abundance in interstitial melt and reprecipitated cpx of variable Al_2O_3 abundance in our reaction couples will allow us to identify the dominant mass transfer processes governing the distribution and partitioning of the high charge, slow diffusing cations during partial melting and melt-rock reaction. One of the major objectives of the present study is to evaluate the extent of chemical equilibrium or disequilibrium between clinopyroxene and its coexisting melt for the REE and HFSE during melt-peridotite interaction. We will show that disequilibrium melting models based on volume diffusion in solid alone are likely to significantly underestimate the rates at which major and trace elements in residual minerals reequilibrate with their surrounding melt.

2. Experimental and analytical methods

2.1 Starting materials

Starting materials for this study were prepared from mineral separates of two fertile spinel lherzolite xenoliths from central Mexico, XDJ-16 and XDJ-11, described by Liang and Elthon (1990). Olivine, cpx, and opx were separated from XDJ-16 and the spinel (sp) was collected from XDJ-11 because of its larger grain size and similar composition to XDJ-16.

For one experiment, we used a basaltic glass from the Herdubreid volcano in Iceland (sample HBT01) in order to increase the Al_2O_3 content of the system. The major element compositions of the starting materials are reported in Table 1.

Coarse mineral separates (0.5-1 mm) were obtained from sieved and optically clean handpicked minerals from the disaggregated nodules. The separates were then ground for 20 minutes in ethanol, dried under a heating lamp and sieved again to obtain a range in grain size of 25-38 μm . Five sets of starting materials were obtained by mixing the processed mineral separates and basaltic glass in desired proportions: (1) pure cpx, (2) opx with less than 5% (by volume) olivine, (3) 54% (by weight) olivine and 46% opx, (4) 94% opx and 6% sp, and (5) 76% cpx, 6% spinel and 17% basaltic glass.

2.2 Experimental methods

All experiments were conducted using a 19.05 mm piston cylinder apparatus using straight-walled graphite furnace, NaCl pressure medium, Pyrex tubing, crushable MgO spacers and insulators, and a molybdenum capsule. The cylindrical molybdenum capsule (6.5 mm OD, 4.1 mm ID, 10 mm long) is lined with a platinum tube (4.0 mm OD, 3.8 mm ID), which in turn is lined with a graphite inner sleeve (3.8 mm OD, 2.0 mm ID), as shown in Fig. 2a. In this assembly the sample is in contact only with the graphite inner sleeve and therefore the oxygen fugacity of the experiments is maintained at or below the graphite-CO buffer, which corresponds to a $\log f\text{O}_2 \leq \text{FMQ-1}$ log unit at 1340°C and 1.5GPa (e.g., Jacobsson and Oskarsson, 1994). One of the advantages of using the Mo-Pt-C capsule is that the strength of Mo assures a reasonably good geometry for both synthesis and dissolution runs, while preventing the sample and the graphite capsule from reacting with the Mo.

Melting experiments were carried out in several steps. First we synthesized the five starting materials in a Mo-Pt-C capsule at 1.5 GPa for 48 hours. Four of the syntheses (cpx, opx, harzburgite, and opx + sp) were run at 1340°C while the synthesis of the cpx + spinel + glass and one set of the opx + spinel mixture were run at 1300°C, due to the lower melting point of the cpx + spinel + glass mixture. After quenching each synthesis run, the capsule was sectioned perpendicular to its cylindrical axis with the exposed surfaces polished down to 1 μm finish and dried for at least 24 hrs at 200°C in a vacuum oven. Cylindrical half-capsules were then juxtaposed and jacketed with a platinum tube to form a reaction couple. Pt and Mo form a solid solution at high pressure and high temperature which helps to prevent the two half capsules from separating during quench. The complete furnace assembly is then stored at 200°C in a vacuum oven again for at least 24 hours before actual melting or reaction experiment.

To conduct a melting experiment, the reaction couple was first cold pressurized to a pressure of ~ 1.6 GPa. The temperature was then raised at a rate of 75°C/min to either 1100°C (for the cpx + spinel + glass vs. opx + spinel assembly) or 1200°C (for all other assemblies). After an annealing period of 24 hours, the temperature was then increased at a rate of 150°C/min to the desired temperature, and held at the run conditions for 72 to 79 hours. The run was quenched to room temperature and the capsules were then mounted in epoxy, sectioned longitudinally, and polished down to 0.3 μm finish for electron microprobe and ion probe analyses. Due to the slight difference in diameters between the two half cylindrical capsules containing the pre-synthesized material, a small offset at the original interface is visible after quench, and is used as a marker for distance measurements. In general the offset between the two half capsules is less than 15-20% of the total width of the sample. Runs with larger offset were not included in this report.

The temperature was monitored using a W₉₇-Re₃/W₇₅-Re₂₅ thermocouple and a Eurotherm 818 controller. No pressure correction was applied to the measured e.m.f. Uncertainties in the temperature measurements were about 10°C due mainly to a temperature gradient in the solid medium assembly (e.g., Ayers et al., 1992; Liang et al., 1996; Watson et al., 2002). The nominal pressure was not corrected for friction because the slight pressure fluctuations (~30 MPa) during a run are comparable to the 25 MPa friction correction measured by Ayers et al. (1992) for a similar furnace assemblage.

2.3 Analytical methods

Backscattered electron (BSE) images, X-ray intensity maps, and mineral and melt chemical analyses were collected at Brown University using a Cameca SX-100 electron microprobe. An accelerating voltage of 20 kV and a beam current of 50 nA were used to collect BSE images and X-ray intensity maps. An accelerating voltage of 15 kV was used for the mineral and glass analyses. A focused beam (1-2 µm) of 20 nA was used for the mineral analyses, and a slightly defocused beam (5 µm) of 10 nA was employed for the glass. Counting times were 20 s for peak and 10 s for background on each side of the peak. Natural glass and mineral standards were used for all analyses and the PAP correction procedure was employed (Pouchou and Pichoir, 1984). To minimize sodium loss during the analyses, Na₂O was analyzed first. Raw oxide sums for the individual analyses were above 98.8 wt.% for minerals and above 95.6 wt.% for the glasses. Grain-size and volume fractions of all the phases present in the reactive boundary layer were measured from BSE images and X-ray intensity maps using the intercept length and point count methods described in Underwood (1970).

In addition, a suite of 11 trace elements (La, Ce, Nd, Sr, Zr, Sm, Ti, Dy, Y, Er, Yb) was determined on the glass and cpx using a Cameca 3f ion probe at the Woods Hole

Oceanographic Institute. Analyses were performed using a 35-40 nA primary beam of O⁻ with a ~20 µm spot size for Sr, Zr, Ti, Y, a ~50 µm spot size for REE, and utilizing secondary ions with an energy filtering window of -60 or -90 volts depending on the trace element analyzed (Shimizu and Hart, 1992).

3. Results

3.1 *Experimental charge*

The samples obtained at the end of each melting experiment are approximately 4-5 mm long and ~1.5 mm in diameter. Reflected light and BSE images of the synthesized starting materials indicate that they typically contained small amounts of melts at the run conditions (up to ~5 vol% for the cpx+sp+glass synthesized rod). The opx synthesis also contained 4-5% olivine probably present in the starting material due to incomplete mineral separation.

Four successful melting runs were obtained at 1.5 GPa using the reaction couple: (1) opx against cpx (Run 37, 1340°C for 72 hours, Fig. 3); (2) opx + spinel against cpx+sp+glass (Run 49, 1300°C for 73 hours); (3) opx + spinel against cpx (Run 54, 1340°C for 72 hours); and (4) olivine + opx against cpx (Run 27, 1340°C for 79 hours, Lo Cascio et al., 2004). Reaction between the cpx-rich lithology and the opx-rich lithology at 1300-1340°C and 1.5 GPa produces a RBL that consists of new olivine, cpx, and melt (\pm spinel depending whether spinel is present in the starting material). The width of these RBL's is about 250 µm for Run 27, 180 µm for Run 37, 200 µm for Run 49, and 240 µm for Run 54. The lithological or mineralogical boundary between the RBL and the unreacted pyroxenite or harzburgite is sharp and planar (Fig. 3), similar to the sharp dunite-harzburgite interface observed in the harzburgite or lherzolite dissolution experiments (e.g., Morgan and Liang,

2003 and 2005). The opx-free RBL is always located on the opx-rich side of the original capsules interface, suggesting that the RBL grows at the expense of opx.

3.2 Textures

Olivine is euhedral to subhedral in the RBL with a median grain size of 40 μm . Clinopyroxene crystals in the RBL are typically anhedral with a median grain size of ~ 60 μm . In areas where olivine grains are abundant, cpx grain-size is typically smaller. We also observe at the edge of the RBL, near the opx-rich side of the capsule, few small anhedral opx grains (5-10 μm in diameter), representing incompletely dissolved opx crystals. In runs where spinel was added to the starting material, there are only few small grains (up to ~ 10 μm) of spinel present in the RBL. These small spinels are usually trapped inside large olivine grains. Far from the RBL, spinel is homogeneously distributed and has a grain size of 20 to 35 μm (Fig. 4). In general, melt in the RBL tends to localize in those areas where olivine grains are more densely accumulated (Fig. 3; see also Fig. 1 of Lo Cascio et al., 2004). Quench growth of cpx is also more abundant in those areas where cpx crystals are more abundant and much less in areas where olivine is present. These help to explain why some melt pockets can be as wide as 150 μm and are less affected by quench growth. The precise grain size of pyroxenes far from the RBL is difficult to determine. Nevertheless, using the melt distribution as a phase boundary and the chemical zonations present in some pyroxenes, it is possible to make a rough estimate of 30-40 μm for opx and cpx in the orthopyroxenite (or harzburgite) and clinopyroxenite, respectively.

3.3 Mineral compositions

Detailed microprobe traverses across all experimental runs show that the composition of olivine is essentially uniform. Opx shows some scatter in composition due

to the presence of grains with unreacted cores but the variation is not related to distance from the RBL (Fig. 5). The compositions of cpx (Figs. 5 and 6, see also Fig. A1 in the supplementary material) and spinel (Fig. 8) vary systematically with distance from the RBL and both minerals have compositional gradients that extend beyond the mineralogical boundaries that define the RBL (Fig. 5, see also an enlarged plot of the boxed area is shown in Fig. A2 in the supplementary materials). In general, the Mg^{2+} , Fe^{2+} and Si^{4+} contents of cpx per six oxygens increase towards the reaction front, whereas Ti^{4+} , Al^{3+} , Cr^{3+} , Ca^{2+} , Na^{+} , REE^{3+} , Y^{3+} , Zr^{4+} , and Sr^{2+} contents decrease (Figs. 5 and 6, see also Fig. A1 in the supplementary materials). Electron microprobe traverses across selected single crystals of cpx show that grains far away from the RBL have systematic core-to-rim variations that account for the scatter in the observed compositional trends away from the RBL (labeled as “core” and “rim” in Figs. 5 and 6). These core-to-rim compositional variations are very similar to those observed in pyroxenes in the unreacted lherzolite in the melt-peridotite reaction experiments of Morgan and Liang (2005, their Figs. 7 and 9). In contrast, compositional variations of cpx in the RBL are more systematic, indicating a lack of significant zoning parallel to the original interface. Compositional traverses across the entire reaction couple also show that the chemical gradients for different elements levels off at approximately the same distance from the original interface, regardless of the size and charge of the cation (Figs. 5 and 6). In addition we observe a linear correlation between cations of different size and charge (Fig. 7), such as Ce^{3+} *vs.* Yb^{3+} and Sr^{2+} *vs.* Zr^{4+} , with low concentrations in the RBL.

The Mg^{2+} and Al^{3+} contents of spinel decrease towards the RBL, whereas the Ti^{4+} , Fe^{2+} , and Cr^{3+} increase. The net effect of these trends on the spinel composition is an increase in the Cr# [molar $100 \times \text{Cr} / (\text{Cr} + \text{Al})$] and a decrease in the Mg# [molar $100 \times \text{Mg} / (\text{Mg} + \text{Fe})$] from the original spinel composition far from the RBL (Mg# ~82 and 85 and Cr# ~10

and 12 for runs 49 and 54, respectively) towards the reaction front (Mg#~79 and 81 and Cr# ~22 and 25 for runs 49 and 54, respectively; Fig. 8). The dominant effect of adding spinel or basalt to the starting material is to increase the average Al₂O₃ content of the bulk starting composition (Fig.5, see also cpx compositions in Run 49 and 54 in Fig. A1), resulting in higher Al₂O₃ content in cpx in the presynthesized starting materials. During the melting reaction, the composition of the cpx in the RBL becomes depleted in Al₂O₃ relative to the cpx composition far from the RBL (Figs. 5 and A1 and A2). For Run 49 where basalt was added to the cpx-rich aggregate in addition to the spinel, clinopyroxene composition is homogeneous throughout the charge, due to faster equilibration during the synthesis run. For Run 54 where spinel was only added to the opx-rich aggregate, the Al₂O₃ abundance in cpx increases from the clinopyroxenite towards the RBL, as a result of spinel dissolution in the RBL. Detailed compositional variations of MgO, FeO, CaO, and Al₂O₃ across the four melting/reaction charges are presented in Fig. 1A in the supplementary materials.

3.4. Melt compositions

Partial melts in the RBL are ne-normative alkali basalts and do not show significant variations in composition with respect to distance (see Fig. 2 of Lo Cascio et al., 2004). However, there is compositional scatter in major elements, reflecting quench modification. The average Fe-Mg exchange coefficient between olivine and melt ($K_d^{\text{Fe-Mg}}$) in our experiments is 0.21 (± 0.04), 0.25 (± 0.03), 0.16 (± 0.02), and 0.13 (± 0.01) for runs 27, 37, 49, and 54, respectively. However this average is not meaningful since the composition of olivine is essentially constant, and the change is due solely to the quench modification in the glass composition. Table 2 shows the average glass, olivine, opx, cpx, and spinel compositions for all runs. The deviation from the mean in the glass composition indicates that quench growth does affect our Fe-Mg exchange coefficient.

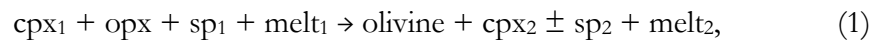
The trace element abundance of the glasses in all runs shows less scatter than major elements, due to the larger volume sampled by the ion probe (~20 to 50 μm wide beam spot, compared to the $< 5 \mu\text{m}$ wide beam of the microprobe) and to the fact that their abundances are less sensitive to quench modifications compared to those of major elements. Table 3 lists selected trace element abundance in cpx and melt located in the RBL, and the apparent cpx-melt apparent partition coefficients (K_d) calculated directly using the measured data. As shown in Fig. 9, the apparent partition coefficients are correlated with the Al^{IV} content of the residual cpx, as has been observed in a number of partitioning studies (e.g., Hart and Dunn, 1993; Hauri et al., 1994; Lundstrom et al., 1994; Gaetani and Grove, 1995; Blundy et al., 1998; Hill et al., 2000; Gaetani, 2004). This point will be further discussed in Section 5.2 below.

4. Grain-Scale Processes of Lherzolite Melting

The presence of concentration gradients in all of our experiments suggests that diffusion plays an important role during the formation of the RBL. The question then is whether the development of the RBL is dominated by diffusion in the solid, in the melt, or by a combination of the two. Given that cation diffusivities in pyroxenes and spinel are very small compared to those in the melt, it is unlikely that the observed cpx and spinel concentration gradients developed over a distance of 200 μm in less than 80 hours are produced by solid-state diffusion alone. For instance, to account for the observed concentration gradients of CaO, MgO, and FeO in the cpx across the RBL, a bulk diffusivity of $\sim 10^{-13}$ – $10^{-15} \text{ m}^2/\text{s}$ would be needed (see Fig. A1 in the supplement materials). This bulk diffusivity for major elements is 3-5 orders of magnitude larger than the Mg^{2+} - Fe^{2+} chemical diffusivity in cpx (Brady and McCallister, 1983) and 3-4 orders of magnitude smaller than the effective binary diffusivities of MgO and FeO in basaltic melt at 1300°C (e.g., Richter et

al., 2003). This indicates that diffusion in both the solid and the melt, via dissolution and reprecipitation, must contribute to the development of the RBL. In addition, textural evidence such as the presence of large olivine crystals in the RBL for runs where minor amounts of olivine were present in the starting material (Run 37, Fig. 3), the absence of opx and decrease in spinel grain-size in the RBL, and the presence of cpx on the side of the capsule where it was initially absent, all suggests that dissolution and precipitation occur simultaneously during the development of the RBL. This grain-scale process is independent of the choice of reaction couples, nor the presence/absence of spinel, and hence common to melt-peridotite interaction in general.

The development of the RBL involves dissolution of cpx, opx, and spinel, followed by reprecipitation of cpx, and precipitation of olivine and is consistent with the following reaction:



where subscripts 1 and 2 designate the presynthesized material before melting and the product in the RBL, respectively. The volume of melt₂ (> 15% within the RBL) is greater than that of melt₁ (< 5% within the cpx-rich capsule), indicating that net melting occurs during this reaction (Fig. 3). The original melt in the clinopyroxenite (melt₁) is undersaturated in opx and spinel and enriched in jadeite component. Hence melt₁ dissolves opx and spinel at the clinopyroxenite-orthopyroxenite or clinopyroxenite-harzburgite reaction front. Incongruent dissolution of opx produces olivine and a silica-rich liquid, while partial dissolution of spinel elevates the Al₂O₃ abundance in the interstitial melt in the RBL (Table 2). Parts of the dissolved opx and spinel components mix with melt₁, resulting in cpx reprecipitation in the RBL (cpx₂, Fig. 3; see also Figs. 1b-1d in Lo Cascio et al., 2004). The composition of melt₂ is the net result of melt₁ and opx + spinel reaction, olivine precipitation, and cpx₂ reprecipitation in the RBL. The composition of spinel is also

significantly affected by dissolution and reprecipitation before reacting out completely (Fig. 8): its Cr# increases while its Mg# decreases towards the RBL, resulting in an increase in the FeO and Al₂O₃ content of the melt in the RBL.

A salient feature of dissolution, precipitation, and reprecipitation is that the rates of opx and spinel dissolution, as well as olivine and cpx₂ precipitation, are limited by the rates of diffusion of the major components in the interstitial melt and the solid (e.g., SiO₂ and Al₂O₃, Liang, 2003b; Morgan and Liang, 2003). Hence, the crystal-melt equilibration time scales in the RBL are significantly reduced, in spite of the expected slow diffusion rates of high charge cations such as REE³⁺, Y³⁺, Ti⁴⁺, and Zr⁴⁺ in pyroxenes (e.g., Van Orman et al., 2001; Cherniak and Liang, 2007; Cherniak and Liang, unpublished data). This helps to explain the large apparent diffusion distances of Sr²⁺, Sm³⁺, and Zr⁴⁺ as well as the nearly linear and positive correlations between Sr²⁺ and Zr⁴⁺ in Figs. 6 and 7.

5. Implications for Trace Element Distribution During Peridotite Melting

Through numerical calculations, theoretical analyses, and laboratory dissolution, melting, and melt-rock reaction experiments (Liang 2003a, 2005; Morgan and Liang, 2003, 2005; Lo Cascio et al., 2004; and this study) we have shown that dissolution, precipitation, and reprecipitation are an inevitable consequence of crystal-melt reaction and reequilibration in multicomponent crystal-melt aggregate. These grain-scale reequilibration processes have important implications for the distribution of major and trace elements in coexisting minerals and melt during melting and melt-rock reaction. Implications for major element compositional zoning in residual pyroxenes observed in isothermal-isobaric partial melting experiments was discussed by Lo Cascio et al. (2004). In this section, we will focus on trace element distributions by considering two examples: one commonly observed in laboratory

melting studies and the other frequently used in modeling studies of disequilibrium mantle melting and melt transport.

5.1. Trace element fractionation during disequilibrium melting in nature

Disequilibrium melting takes place when the rate of melting is greater than the rate of solid-melt chemical exchange, through volume diffusion in the solid and/or dissolution and reprecipitation. For an incompatible trace element, this can be conveniently measured by a dimensionless melting Damköhler number, (e.g., Liang, 2003a; Cherniak and Liang, 2007),

$$D_m^k = \frac{[\rho_f \phi + \rho_s (1 - \phi)] k R}{\Gamma} \quad (2)$$

where ρ_f and ρ_s are the densities of the melt and solid, respectively; ϕ is the volume fraction of melt in the residuum; k is the mineral-melt partition coefficient for the element of interest; Γ is the rate of melting of the bulk matrix as defined by McKenzie (1984); and R is the chemical exchange rate between the solid and the melt for a given element of interest. The melting Damköhler number in Eq. 2 was obtained from an analysis of the disequilibrium dynamic melting model of Liang (2003a). It can be shown that disequilibrium melting is important for the incompatible trace element of interest when $D_m^k < 1$.

Previous studies of trace element distribution during disequilibrium mantle melting focused almost exclusively on cases in which the rate of crystal-melt mass exchange is limited by the rate of volume diffusion in the solids (e.g., Qin, 1992; Iwamori, 1993, 1994; Van Orman et al., 2002). The crystal-melt chemical exchange rate in this case can be estimated using the simple expression (e.g., Vermeulen, 1953),

$$R = \frac{\beta D_s}{a^2} \quad (3)$$

where a is the average grain size or radius of the mineral of interest; D_s is diffusion coefficient in the mineral for the element of interest; and β is a geometry factor ranging from 3 to 15 (e.g., Vermeulen, 1953; Navon and Stolper, 1987; Bodinier et al., 1990; Liang, 2003b). Since diffusion is a thermally activated process one would expect that disequilibrium melting plays an important role at moderate to low temperatures ($< 1100^\circ\text{C}$). Such environments can be found during wet or flux melting in the upper mantle or lower crust, where the solidi of the mantle or crust materials are low and the rates of volume diffusion in residual minerals are small. Consider an example of REE fractionation during wet melting of a peridotite at 1100°C and 2 GPa. Van Orman et al. (2002a) and Cherniak and Liang (2007) measured the diffusion coefficients of REE in diopside and enstatite, respectively. Assuming a grain size of 1 mm, a bulk density normalized melting rate of 10^{-14} to 10^{-15} s^{-1} (e.g., Iwamori, 2000), the melting Damköhler numbers are approximately 0.1 to 1 for the REE in enstatite, and 0.01 to 0.1 for La and 1 to 10 for Yb in diopside. Hence a significant component of disequilibrium melting would be expected for the LREE during wet melting of peridotite if volume diffusion in solid were the dominant mass transfer mechanism for crystal-melt chemical exchange. Using a similar argument, we have recently shown that the effect of diffusion in solid limited disequilibrium melting can still be observed for the REE in melts produced by dehydration melting of a subducting slab even when the grain sizes of garnet and cpx in the residual eclogite are as small as $100 \mu\text{m}$ (Liang, 2003a). In spite of these theoretical predictions, significant components of disequilibrium melting have not been reported for the REE in magmas produced in the aforementioned tectonic settings. This, of course, does not rule out the possibility of diffusion in solid limited disequilibrium melting in either tectonic environment. The paucity of trace element data in support of disequilibrium melting, however, does imply that other mass transport processes such as dissolution and reprecipitation are likely to play a dominant role in distributing and

equilibrating slow diffusing species between residual minerals and their surrounding melt during partial melting. As discussed in Section 4, dissolution, precipitation, and reprecipitation are most likely to occur during disequilibrium melting of solid solution forming minerals (Liang, 2003a, 2003b, 2005; Lo Cascio et al., 2004; and this study). These grain-scale processes significantly accelerate the rates at which slow diffusing cations in residual minerals reequilibrate with their surrounding melt. Disequilibrium melting models based on volume diffusion in solid alone are likely to significantly underestimate the rates at which major and trace elements in residual minerals reequilibrate with their surrounding melt. This can be further demonstrated by the apparent trace element partition coefficients for cpx and its coexisting melt in the RBL in Section 5.2.

One simple way to incorporate dissolution and reprecipitation into the disequilibrium melting models is to replace the average grain size, a , in Eq. 3 by an effective grain size that is defined as the average size of the unreacted cores of a mineral of interest. Although dissolution and reprecipitation can increase mineral grain size, as demonstrated in this study, it is the regions that are not affected by reprecipitation (i.e., mineral cores) that are likely to be significantly out of chemical equilibrium with the surrounding melt during melt-rock interaction. This approach was used by Liang (2003a) in his study of disequilibrium melting of a subducting slab. The effective grain size can be significantly smaller than the actual grain size (Liang, unpublished numerical results). Further studies are needed to constrain the effective grain size during mantle melting and melt-peridotite interaction.

5.2. Apparent clinopyroxene-melt trace element coefficients from this study

Partition coefficient of incompatible trace element between cpx and basaltic melt is a critical parameter to understand melting and melt transport processes in the upper mantle (e.g., Blundy and Wood, 2003 and references therein). Although in principle one could

measure the elemental abundance in coexisting cpx and melt after a peridotite partial melting experiment, it has never been done before due to analytical difficulties such as small crystal and melt pocket sizes, crystal zoning, as well as quench modification. This is the main reason why the trace element partition coefficients between cpx and melt are generally determined through crystal growth experiments. According to the dissolution and reprecipitation processes discussed in Sections 4, it is reasonable to assume that the large cpx grains in the RBL produced in our reaction couple experiments are compositionally equivalent to the cpx rim in bulk lherzolite melting studies. An important question then is how far the apparent cpx-melt partition coefficients reported in this study (Table 3 and Fig. 9) deviate from the cpx-melt (equilibrium) partition coefficients obtained by other experimental methods (e.g., cpx crystallization in controlled cooling experiments). Here the word “apparent” is used to distinguish our measured cpx-melt partition coefficients from the equilibrium partition coefficients. The former is identical to the latter when chemical equilibrium is established.

It is well known that cpx-basaltic melt partition coefficients for REE and HFSE depend strongly on the abundance of tetrahedrally coordinated Al (Al^{IV}) in cpx, whereas cpx-melt partition coefficient for Sr is insensitive to the Al^{IV} abundance in cpx (e.g., McKay, 1986; Hart and Dunn, 1993; Hauri et al., 1994; Lundstrom et al., 1994; Gaetani and Grove, 1995; Blundy et al., 1998; Hill et al., 2000; Gaetani, 2004). Figure 9 shows the cpx-melt partition coefficients for REE, Y, Ti, Zr, and Sr as a function of Al^{IV} abundance in cpx reported in recent laboratory partitioning studies (references given in the caption to Fig. 9). Deviations from the general trends among the published data shown in this figure could be due to differences in melt composition, temperature and pressure, as well as experimental and analytical uncertainties among different studies. For comparison, we also plot the cpx-melt apparent partition coefficients obtained from our reaction couple experiments, shown

as larger symbols in Fig. 9. In general, our apparent partition coefficients agree reasonably well with the published values. In detail, however, we note that our apparent partition coefficients for larger ions (La, Ce, Sr, and to a lesser extent, Nd) and Ti in Runs 27 (large red circle) and 37 (large blue circle, Fig. 9) are slightly but systematically lower than the general trends established by other partitioning studies. It is unlikely that these lower than expected apparent partition coefficients are a result of analytical error, given the similarities in the major and trace element abundance between Runs 27 and 37. Possible explanations for this deviation include (1) differences in melt composition between our study and other partitioning studies; (2) fast cpx growth or precipitation rate in the RBL; (3) ionic charge and size dependent cation diffusion in cpx; and (4) incomplete crystal-melt reequilibration in the RBL in spite of dissolution and reprecipitation. We will briefly address each possible cause below.

Both Gaetani et al. (2003) and McDade et al. (2003) have shown that the presence of more than 1 wt% of H₂O in coexisting silicate melt can reduce the cpx-melt partition coefficients for the REE and HFSE relative to values obtained from anhydrous partitioning studies. Gaetani (2004) has further demonstrated that cpx-melt partition coefficients for the REE also depend on melt structure and hence melt composition. According to these studies, variations in melt composition not only affect the cpx-melt partition coefficients for the light REE (LREE) but also the mid to heavy REE and the HFSE, which is not the case in the present study: our apparent partition coefficients for the LREE are lower than the systematic trend established by the published data, whereas our apparent cpx-melt partition coefficients for the mid to heavy REE, Y, and Zr are in good agreement with the published data (Fig. 9). Although the exact amount of H₂O in the melt coexisting with cpx in our experimental charges is not known, we conclude that differences in melt composition are unlikely the cause to the systematic deviations shown in Fig. 9.

It is well known that fast crystal growth can lead to trapping or enrichment of slow diffusing incompatible trace elements in a growing crystal. The amount of enrichment are positively correlated with the growth Péclet number (e.g., Aziz, 1982; Watson and Liang, 1995), a dimensionless number that measures the relative crystal growth rate to the trace element diffusion rate across the near surface layer of the crystal. The run duration and cpx crystal size in the RBL in our reaction couple experiments are comparable to those reported in crystal growth/partitioning studies. Hence it is unlikely the reprecipitation rate of cpx in the RBL in our reaction couple experiments is significantly different from those in other partitioning studies. Furthermore, near surface trapping always results in an increase in the apparent crystal-melt partition coefficient for the incompatible trace elements (e.g., Aziz, 1982; Watson and Liang, 1995), which is the opposite of the systematic deviation observed in this study.

Van Orman et al. (2001) have shown that tracer diffusivities of the REE in diopside increase systematically from La to Lu. Hence it is possible that the lower than expected apparent partition coefficients for La, Ce, and Nd obtained from our reaction couple experiments are due to the slow diffusion rates of these elements relative those of the mid to heavy REE and Y in cpx, despite of dissolution and reprecipitation in the RBL. Although tracer diffusivities of Ti and Zr in cpx have not been measured directly, trace element zoning patterns preserved in cpx in plagioclase lherzolite from Horoman peridotite (Takazawa et al., 1996) suggest that the apparent or effective diffusivity of Ti in cpx is smaller than the apparent diffusivity of Zr in cpx. Typically, the width of the concentration boundary layer thickness for Ti in cpx in Horoman plagioclase lherzolite is comparable to that for Nd in the cpx, but the concentration boundary layer thickness for Zr in cpx is comparable to those for Dy, Y, and Er in the same cpx (see Figs. 4 and 5 in Takazawa et al., 1996). Hence it is possible that the apparent diffusivity of Zr in cpx is larger than the apparent diffusivity of Ti

in cpx. This may help to explain our lower than expected apparent partition coefficient of Ti but effectively normal partitioning behavior of Zr in Runs 27 and 37.

It is well known that tracer diffusivity of Sr in diopside is significantly larger than those of REE in diopside (e.g., Sneeringer et al., 1984). If sluggish diffusion of Sr in cpx is significant in affecting its reequilibration time, then why does it not affect the HREE whose diffusivities are smaller than that of Sr in cpx? The answer probably lies in the cpx-melt partition coefficient. Hart (1993) pointed out that diffusive reequilibration time for a trace element in crystal-melt aggregate also depends on crystal-melt partition coefficient. This is why the melting Damköhler number defined in Eq. 2 is also a function of partition coefficient. According to Hart (1993) and our numerical calculations (Liang, unpublished results), the crystal-melt reequilibration time is longer for more incompatible trace element than for less incompatible one, though its exact functional form depends on boundary conditions and whether other transport processes such as melting, advection, and melt-rock reaction also present during crystal-melt diffusive reequilibration. Given the relative small cpx-melt partition coefficient for Sr (0.06, according to Fig. 9) compared to HREE, it is possible that the cpx-melt reequilibration time for Sr is slightly longer than that for the HREE such that Sr has still not fully equilibrated at the end of our experiments.

The lower than expected apparent partition coefficients of La, Ce, Sr, and to a lesser extent, Nd and Ti in Runs 27 and 37 can be understood in terms of the grain scale processes discussed in Section 4 and in Lo Cascio et al. (2004). Partial melting of the fertile clinopyroxenite during both synthesis and melting reaction experiments produced an incompatible element enriched melt (melt₁ in Eq. 1). Reaction between melt₁ and opx produced a RBL that consists of precipitated olivine and cpx (cpx₂ in Eq. 1) and an incompatible element depleted melt (melt₂ in Eq. 1). Because the depleted melt₂ in the RBL exchanges chemically with the enriched melt₁ in the clinopyroxenite via diffusion through

interstitial melt, its incompatible trace element abundance is elevated relative to the melt at the RBL-orthopyroxenite or RBL-harzburgite interface. If diffusion in the near surface region of cpx₂ cannot keep up with melt₁-melt₂ diffusive exchange in the growing RBL, the apparent cpx-melt partition coefficients for the incompatible trace elements will be lower than their equilibrium values. An important implication of this open system behavior is that dissolution and reprecipitation, though significantly faster than simple solid state diffusion in minerals, are still not fast enough on laboratory time scales such that small but measurable amounts of disequilibrium between reprecipitated cpx and its coexisting melt can still exist, especially for the highly incompatible trace elements. Depending on the time scale of magmatic processes, grain-scale isotopic and chemical heterogeneities can be preserved at least in some mantle rocks.

6. Summary and Conclusions

We have shown that partial melting of lherzolite of varying bulk compositions can be studied in great detail by analyzing the formation of a reactive boundary layer between cpx-rich and opx-rich aggregates, as long as the peridotite melting reaction consumes pyroxenes and produces olivine and melt. We found that the RBL growth at constant temperature and pressure takes place by melting, and by dissolution and reprecipitation of several phases. These grain-scale processes significantly reduce the diffusive equilibration time between solid-solution forming minerals and the surrounding melt and affect the distribution of major and trace elements, especially for cations with relatively slow diffusion coefficients. We showed that during mineral-melt equilibration, volume diffusion in minerals is not the dominant mechanism of chemical exchange, but rather dissolution and reprecipitation. This conclusion led us to speculate that these grain-scale processes might be responsible for the lack of disequilibrium melting component in arc magmas and melts from

back arc basins. Detailed analysis of coexisting cpx and melt in our runs also show that the cpx/melt partition coefficient for incompatible trace elements is primarily controlled by the Al^{IV} content of the cpx, as noted in previous studies. However, for larger cations and Ti we observe a partition coefficient lower than expected, indicating that dissolution and reprecipitation are not fast enough to eliminate completely small degrees of disequilibrium during our experiments. Depending on the timescale of melting and melt migration relative to the timescale of melt-rock reequilibration, chemical and isotopic heterogeneities can be preserved in mantle rocks.

Acknowledgements

This paper has benefited from discussions with Alberto Saal, as well as comments from two anonymous reviewers. This work was supported by NSF grants EAR-0208141 and EAR-0510606 to Yan Liang.

References

- Ayers JC, Brenan JB, Watson EB, Wark DA, Minarik WG (1992) A new capsule technique for hydrothermal experiments using the piston-cylinder apparatus. *Am Mineral* 77: 1080-1086
- Aziz MJ (1982) Model for solute redistribution during rapid solidification. *J Appl Phys* 53 (2): 1158–1168
- Blundy JD, Robinson JAC, Wood BJ (1998) Heavy REE are compatible in cpx on the spinel lherzolite solidus. *Earth Planet Sci Lett* 160: 493-504
- Blundy J, Wood B (2003) Partitioning of trace elements between crystal and melts. *Earth Planet Sci Lett* 210: 383-397

- Bodinier JL, Vasseur G, Vernieres J, Dupuy C, Fabries J (1990) Mechanisms of mantle metasomatism: Geochemical evidence from the Lherz orogenic peridotite. *J Petrol* 31: 597–628
- Brady JB, McCallister RH (1983) Diffusion data for clinopyroxenes from homogenization and self-diffusion experiments. *Am Mineral* 68: 95–105
- Cherniak DJ, Liang Y (2007) Rare earth element diffusion in natural enstatite. *Geochim Cosmochim Acta* 71: 1324-1340
- Gaetani GA (2004) The influence of melt structure on trace element partitioning near the peridotite solidus. *Contrib Mineral Petrol* 147: 511-527
- Gaetani GA, Kent AJR, Grove TL, Hutcheon ID, Stolper EM (2003) Mineral/melt partitioning of trace elements during hydrous peridotite partial melting. *Contrib Mineral Petrol* 145 (4): 391–405
- Gaetani GA, Grove TL (1995) Partitioning of rare earth elements between cpx and silicate melt: Crystal-chemical controls. *Geochim Cosmochim Acta* 59: 1951–1962
- Hart SR (1993) Equilibration during mantle melting: A fractal tree model. *Proc Natl Acad Sci* 90: 11914–11918
- Hart SR, Dunn T (1993) Experimental cpx/melt partitioning of 24 trace elements. *Contrib Mineral Petrol* 113: 1-8
- Hauri EH, Wagner TP, Grove TL (1994) Experimental and natural partitioning of Th, U, Pb and other trace elements between garnet, cpx and basaltic melts. *Chem Geol* 117: 149-166
- Hauri EH (1997) Melt migration and mantle chromatography, 1: simplified theory and conditions for chemical and isotopic decoupling. *Earth Planet Sci Lett* 153: 1–19
- Hill E, Wood BJ, Blundy JD (2000) The effect of Ca-Tschermaks component on trace element partitioning between cpx and silicate melt. *Lithos* 53: 203-215

- Iwamori H (1993) Dynamic disequilibrium melting model with porous flow and diffusion-controlled chemical equilibration. *Earth Planet Sci Lett* 114: 301–313
- Iwamori H (1994) ^{238}U – ^{230}Th – ^{226}Ra and ^{235}U – ^{231}Pa disequilibria produced by mantle melting with porous and channel flows. *Earth Planet Sci Lett* 125: 1–16
- Iwamori H (2000) Thermal effects of ridge subduction and its implications for the origin of granitic batholith and paired metamorphic belts. *Earth Planet Sci Lett* 181 (1-2): 131–144
- Jacobsson S, Oskarsson N (1994) The system C-O in equilibrium with graphite at high pressure and temperature: An experimental study. *Geochim Cosmochim Acta* 58: 9–17
- Korenaga J, Kelemen PB (1998) Melt migration through the oceanic lower crust: a constraint from melt percolation modeling with finite solid diffusion. *Earth Planet Sci Lett* 156 (1-2): 1–11
- Liang Y, Elthon D (1990) Geochemistry and petrology of spinel lherzolite xenoliths from Xalapasco de la Joya, San Luis Potosi, Mexico; partial melting and mantle metasomatism. *J Geophys Res* 95: 15,859–15,877
- Liang Y, Richter FM, Watson EB (1996) Diffusion in silicate melts: II. Multicomponent diffusion in CaO-Al₂O₃-SiO₂ at 1500°C and 1 GPa. *Geochim Cosmochim Acta* 60:5021-5035
- Liang Y (2003a) On the thermo-kinetic consequences of slab melting. *Geophys Res Lett* 30: DOI 10.1029/2003GL018969
- Liang Y (2003b) Kinetics of crystal-melt reaction in partially molten silicates: 1. Grain scale processes, *Geochem Geophys Geosyst* 4: DOI 10.1029/2002GC000375
- Liang (2005) Diffusion and reaction in multicomponent partially molten silicates: Dissolution-reprecipitation. *Geochim Cosmochim Acta* 69, Supplement, A177

- Lo Cascio M, Liang Y, Hess PC (2004) Grain-scale processes during isothermal and isobaric melting of lherzolite. *Geophys Res Lett* 31: DOI 10.1029/2004GL020602
- Lundstrom CC, Shaw HF, Ryerson FJ, Phinney DL, Gill JB, Williams Q (1994) Compositional controls on the partitioning of U, Th, Ba, Pb, Sr, and Zr between cpx and haplobasaltic melts: implications for uranium series disequilibria in basalts. *Earth Planet. Sci. Lett* 128: 407-423
- Lundstrom CC, Shaw HF, Ryerson FJ, Williams Q, Gill J (1998) Crystal chemical control of cpx-melt partitioning in the Di-Ab-An system: Implications for elemental fractionations in the depleted mantle. *Geochim Cosmochim Acta* 62: 2849-2862
- McDade P, Blundy JD, Wood BJ (2003) Trace element partitioning on the Tinaquillo lherzolite solidus at 1.5 GPa. *Phys Earth Planet Int* 139: 129-147
- McKay G, Wagstaff J, Yang S-R (1986) Cpx REE distribution coefficients for shergottites: The REE content of the Shergotty melt. *Geochim Cosmochim Acta* 50: 927-937
- McKenzie D (1984) The generation and compaction of partially molten rock. *J Petrol.* 25, 713–765
- Morgan Z, Liang Y (2003) An experimental and numerical study of the kinetics of harzburgite reactive dissolution with applications to dunite dike formation. *Earth Planet Sci Lett* 214: 59–74
- Morgan Z, Liang Y (2005) An experimental study of the kinetics of lherzolite reactive dissolution with applications to melt channel formation. *Contrib Mineral Petrol* 150: 369–385
- Navon O, Stolper E (1987) Geochemical consequences of melt percolation—the upper mantle as a chromatographic. *J Geol* 95: 285–307
- Pouchou JL, Pichoir F (1984) A new model for quantitative x-ray microanalysis 1. Application to the analysis of homogeneous samples. *Recherche Aerospatiale*: 167–192

- Qin Z (1992) Disequilibrium partial melting model and its implications for trace element fractionations during mantle melting. *Earth Planet Sci Lett* 112: 75–90
- Richter FM, Davis AM, DePaolo DJ, and Watson EB (2003) Isotope fractionation by chemical diffusion between molten basalt and rhyolite. *Geochim Cosmochim Acta* 67: 3905–3923
- Salters VJM, Longhi JE (1999) Trace element partitioning during the initial stages of melting beneath mid-ocean ridges. *Earth Planet Sci Lett* 166: 15–30
- Salters VJM, Longhi JE, Bizimis M (2002) Near mantle solidus trace element partitioning at pressures up to 3.4 GPa. *Geochem Geophys Geosyst* 3: DOI 10.1029/2001GC000148
- Shimizu N, Hart SR (1982) Applications of the ion microprobe to geochemistry and cosmochemistry. *Ann. Rev. Earth Planet. Sci.* 10: 483-526
- Skulski T, Minarik W, Watson EB (1994) High-pressure experimental trace-element partitioning between clinopyroxene and basaltic melts. *Chem Geol* 117: 127–147
- Sneeringer M, Hart SR, Shimizu N (1984) Strontium and samarium diffusion in diopside. *Geochim Cosmochim Acta* 48: 1589–1608
- Takazawa E, Frey FA, Shimizu N, Obata M (1996) Evolution of the Horoman peridotite (Hokkaido, Japan): implications from pyroxene compositions. *Chem Geol* 134: 3–26
- Underwood EE (1970) Quantitative stereology. Addison-Wesley, Reading, pp 274
- Van Orman JA, Grove TL, Shimizu N (2001) Rare earth element diffusion in diopside; influence of temperature, pressure, and ionic radius, and an elastic model for diffusion in silicates. *Contrib Mineral Petrol* 141: 687–703
- Van Orman JA, Grove TL, Shimizu N (2002a) Diffusive fractionation of trace elements during production and transport of melt in Earth's upper mantle. *Earth Planet Sci Lett* 198: 93–112

- Vermeulen T (1953) Theory of irreversible and constant-pattern solid diffusion. *Industrial and Engineering Chemistry* 45: 1664–1670
- Walter MJ (2005) Melt extraction and compositional variability in mantle lithosphere. In: Carlson RW (ed) *The Mantle and Core, Treatise on Geochemistry*, 2: 363–394
- Watson EB, Wark DA, Price JD, VanOrman JD (2002) Mapping the thermal structure of solid-media pressure assemblies. *Contrib Mineral Petrol* 142: 640–652
- Watson EB, Liang Y (1995) A simple model for sector zoning in slowly grown crystals; implications for growth rate and lattice diffusion, with emphasis on accessory minerals in crustal rocks. *Amer. Mineral.* 80: 1179-1187
- Watson EB, Othman DB, Luck JM, and Hofmann AW (1987) Partitioning of U, Pb, Cs, Yb, Hf, Re and Os between chromian diopsidic pyroxene and haplobasaltic liquid. *Chem Geol* 62: 191–208
- Wood BJ, Trigila R (2001) Experimental determination of aluminous clinopyroxene-melt partition coefficients for potassic liquids, with application to the evolution of the Roman province potassic magmas. *Chem Geol* 172: 213–223
- Zhang Y, Walker D, Leshner CE (1989) Diffusive crystal dissolution. *Contrib Mineral Petrol* 102: 492–513

Figure Captions

Figure 1. Schematic binary phase diagram showing the processes of dissolution and reprecipitation. Fields of solid solutions are labeled as α_{ss} and β_{ss} . The initial melt and crystal compositions are at L and S, respectively. The final equilibrium crystal and melt compositions are at S_e and L_e , respectively, and are fixed at a given temperature and pressure. See text for details.

Figure 2. Schematic diagram showing the platinum-molybdenum-graphite capsule (a) and the four types of melting couples used in this study (b). The sample is only in contact with graphite.

Figure 3. (a) Back-scattered electron image of the central part of Run 37 (cpx vs. opx \pm ol, 72 hours at 1340°C, 1.5 GPa). (b) False colored X-ray intensity map of Mg corresponding to the same area. Red represents high concentrations (ol) and dark blue represents low concentrations (melt). Light to medium blue corresponds to the cpx from the reactive boundary layer (RBL, center) and far field (top). The yellow area represents the opx grains in the lower capsule. The RBL is confined in between the two dashed lines in (a). The upper dashed line marks the approximate location of the initial interface of the reaction couple.

Figure 4. Backscattered electron image of spinel (sp) in the reactive boundary layer (a), and in the clinopyroxenite, far away from the RBL (b). The spinel grains in the RBL are completely dissolved into the melt unless olivine and/or cpx crystallize around them.

Figure 5. Plots of selected cation concentration per six oxygen for cpx (circles) and opx (triangles) as a function of distance for runs 37 (cpx vs. opx) and 49 (cpx+sp+gl vs. opx+sp). The origin ($x = 0$) marks the initial location of the interface position between the two half capsules. Note that far away from the origin, the

composition of cpx is scattered due to core-to-rim zonation (shown as arrows). However, the composition of the cpx in the RBL is distinct from this chemical variation. The dashed region in the cpx composition is enlarged in the supplementary material (Fig. A2) where the RBL and concentration gradient widths are compared.

Figure 6. Plot of selected trace element abundance (normalized to C1 chondrite) of cpx (circles) as a function of distance for runs 27 (cpx vs. opx+ol) and 37 (cpx vs. opx \pm ol). The origin ($x = 0$) marks the initial location of the interface position between the two half capsules. The data was not collected for single grains but as traverses across the capsule and we observed that some large cpx grains are typically enriched in incompatible elements (“cores”) and that smaller grains are depleted in those elements (“rims), indicating local effects of dissolution and reprecipitation. The numbers shown in the panels represent apparent diffusion coefficients determined by least squares fits to the measured data using an error function solution that includes the movement of the reaction couple interface (e.g., Zhang et al., 1989).

Figure 7. Covariation of Ce^{3+} and Yb^{3+} (a), and Zr^{3+} and Sr^{2+} (b), in cpx from runs 27 and 37. The positive correlation between light and heavy REE, and between cations of very different charge cannot be explained by volume diffusion in cpx. The nearly linear correlations between the light and heavy REE, and between cations of different charge can be explained by a grain-scale process that involves dissolution and reprecipitation (see text a detailed discussion).

Figure 8. Plot of Mg# of spinel vs. Cr# of spinel. Melting and melt-rock reaction decrease the Mg# and increase the Cr# of spinel in the RBL (data enclosed in the dashed ellipses). Trends of melt-rock reaction are shown as an arrow.

Figure 9. Variation of cpx/melt partition coefficients for selected trace elements as a function of the Al^{IV} content in the residual cpx of this study and other partitioning studies. This logarithmic correlation is not observed for Na^+ , Ca^{2+} , or any other cation present in the cpx structure, indicating that the Ca-Tschermak substitution dominates the REE partitioning as suggested by previous studies (e.g., Hauri et al., 1994). The wide range of P-T conditions and melt compositions of the selected partitioning studies, indicates that pressure, temperature, and melt composition do not control directly the REE cpx/melt K_d directly but affect instead the Al^{IV} content of cpx. The Al^{IV} content of cpx is most likely the dominant control on the REE content that can be accommodated in the cpx structure.